The relationship between photoluminescence emissions and photocatalytic activity of CeO_2 nanocrystals

H. Moreno[1*], G. L. Domingues[1], M. Assis[2], P. P. Ortega[1], V.R. Mastelaro[3], M. A. Ramirez[1], A. Z. Simões[1].

1. São Paulo State University – UNESP, School of Engineering and Science, Av. Dr. Ariberto Pereira da Cunha 333, Portal das Colinas, Guaratingueta, São Paulo, Brazil.
2. Department of Analytical and Physical Chemistry, University Jaume I (UJI), Av. Vicent Sos Baynat s/n, Castelló, 12071, Spain.
3. São Carlos Institute of Physics, University of São Paulo, 13566-590 São Carlos, Brazil

*Corresponding author: hpiccolimoreno@gmail.com

ABSTRACT

In this work, we focus on understanding the morphology and photocatalytic properties of CeO_2 nanocrystals (NCs) synthesized via microwave-assisted solvothermal method using acetone and ethanol as solvents. *Wulff* constructions reveal a complete map of available morphologies and a theoretical-experimental match with octahedral nanoparticles obtained through synthesis using ethanol as solvent. NCs synthesized in acetone show greater contribution of emission peaks in the blue region (~450 nm), which may be associated with higher Ce^{3+} concentration, originating shallow-level defects within the CeO_2 lattice while for the samples synthesized in ethanol a strong orange-red emission (~595 nm) suggests that oxygen vacancies may originate from deep-level defects within the optical bandgap region. CeO_2 synthesized in acetone superior photocatalytic response compared to that of CeO_2 synthesized in ethanol may be associated with an increase in long-/short-range disorder within the CeO_2 structure, causing the E_{gap} value to decrease and facilitating light absorption. Furthermore, surface (100) stabilization in samples synthesized in ethanol may be related to low photocatalytic activity. Photocatalytic degradation was facilitated by the generation of •OH and $\bullet O_2^-$ radicals as corroborated by the trapping experiment. The mechanism of enhanced photocatalytic activity has been proposed suggesting that samples synthesized in acetone tend to have lower e'—$h^{\bullet}$ pair recombination, which is reflected in their higher photocatalytic response.

Keywords: CeO_2 nanocrystals. Wulff construction. Microwave-Assisted Solvothermal.

1. Introduction

Controlling physico-chemical properties of crystalline materials remains a challenge for many technological and scientific applications. Crystal morphology is largely associated with the stability of exposed surfaces, which can be described by their surface energies[1–4]. The reason behind morphology-dependent properties is still unclear and, thus, a theoretical-experimental approach can help make functional materials more efficient from synthesis to application. Cerium dioxide (CeO_2), or ceria, is one of the most reactive rare earth oxides. It shows excellent properties needed for fabricating resonators, antennas, and filters, such as: low dielectric loss and improved $Q \times f$ property associated with relatively high dielectric constant values (ε~29.41), and wide theoretical bandgap energy (E_{gap}=6.0 eV)[5–8]. Due to its unique combination of properties, CeO_2 stands out as an important multifunctional material with applications as gas sensors[7,8], oxygen permeation membranes[9,10], catalysts[11], solar cellsmiller[12–14], coatings[15–17], and biomedicine[18,19]. Its characteristic optical absorption edge associated with its broadband photoluminescent (PL) emission in the visible region and ferromagnetic activity, observed in nanostructured CeO_2, also make it suitable for optoelectronics[7,20] and spintronics[21] applications.

Several methods have been used to synthesize CeO_2 nanocrystals (NCs), *e.g.,* co-precipitation[22], polymeric precursor[23], flow method[24], metalorganic chemical vapor deposition (MOCVD)[25], sol-gel[26], conventional hydrothermal (CH)[27,28], microwave-assisted hydrothermal (MAH)/solvothermal[29–33], etc. CH and MAH methods stand out for enabling ceramic oxide synthesis at low temperatures (below 200°C), which reduces time and energy consumption[34]. Additionally, the morphology of particles can be controlled by carefully setting up the synthesis parameters, such as solvent type, mineralizer, solute concentration, temperature, time, pressure and pH[35]. MAH is a convenient, fast, and cost-effective method that uses microwaves to improve crystallization kinetics by one to two orders of magnitude in comparison with CH. MAH is based on the same principle applied in the microwave-assisted solvothermal (MAS) method; nonetheless, the latter uses solvents other than water (*e.g.*, alcohols or glycols). Varying synthesis parameters it is possible to modify the morphology of CeO_2 NCs to produce nanowires, nanoflowers, and nanocubes[36]. Morphology depends on the way microwave energy is converted into thermal energy during synthesis, which can be measured by the solvent dielectric loss ($tan\delta$)[32]. For instance, considering a conventional microwave oven (f≈2.45 GHz) ethanol is considered a high-$tan\delta$ solvent ($tan\delta$=0.941), while water is mid-$tan\delta$ ($tan\delta$=0.123) and acetone low-$tan\delta$

(*tanδ*=0.054)[37,38]. Hence, solution is heated quicker in the presence of a high-*tanδ* solvent (*i.e.,* ethanol when compared to water or acetone).

In previous studies, our group has optimized the synthesis of pure and doped ceria using MAH. Deus *et al.*[39] investigated the influence of different basic environment and reaction time to synthesize CeO_2 NCs and found out that the synthesis performed at 100°C for 8 minutes with KOH and NaOH resulted in higher crystallinity and lower aggregation. Amoresi *et al.*[40] and Oliveira *et al.*[41] prepared different morphologies of CeO_2 NCs by controlling the basic environment concentration and reaction time, obtaining nanocubes, nanobeans, nanorods, nanohexagons, and nanowires. Rare-earth (Pr, Eu, and La) doped ceria nanoparticles were also synthesized via MAH, and the dopant influence on the optical, magnetic, and gas sensing properties of ceria was studied[42,43]. However, to the best of our knowledge the effect of solvents other than water on the properties of ceria nanostructures has not yet been investigated.

Theoretical studies have been tremendously successful in predicting the properties of atomic, molecular, and condensed matter systems and have been well standardized owing to a profound agreement with experimental results. Based on this, our group combined computational simulations and experimental analyzes in an attempt to correlate morphology and properties, which could be the key to improve micro/nanomaterial applications, such as ZnO[44], Ag_3PO_4[45], a-Ag_2WO_4[46,47], $PbMoO_4$[48], $ZnWO_4$[49,50]. These studies point out that targeting the synthesis of facet-dependent nanostructures may be a promising tool to select morphologies with superior optical and photocatalytic properties. Overall, our group aims to narrow the knowledge gap between experiment and theory, demonstrating how understanding the morphology could pave the way to develop and/or enhance optical and photocatalytic properties of nanostructured materials[51,52].

In this paper, we investigated the morphology and photocatalytic of CeO_2 NCs synthesized via the MAS method using acetone and ethanol as solvents. The morphology was evaluated and correlated with the PL and photocatalytic of the samples to better describe the mechanisms behind PL emissions and factors such as photocatalyst particle size, electrostatic attraction between the particle and dye molecule which determine the adsorption behavior of a material. Solvent-induced structural defects and crystal morphology (experimental and theoretical) were evaluated to understand the effect of polarity, solubility, and dielectric loss of acetone and ethanol in the formation of CeO_2 NCs. Relation between surface energy and solvent-induced defects was considered for proposing an electronic structure model and its associated PL emission mechanism.

Hence, we provide theoretical-experimental evidence to support the use of CeO_2-based ceramics in optoelectronic and photocatalytic devices. To the best of our knowledge, such an approach to CeO_2 NCs synthesized via MAS with different solvents has not been yet carried out and may be significant to understanding surface-dependent photocatalytic and PL properties.

2. Experimental section

2.1 CeO_2 nanocrystal synthesis

CeO_2 nanocrystal synthesis (NCs) were prepared via MAS using two different solvents: ethanol and acetone. The MAS method was used due to its successive dissolution/recrystallization processes, which are triggered by microwave irradiation, thus, allowing a quicker, highly reproducible/controlled defect structure to be formed. First, cerium nitrate hexahydrate ($CeNO_3.6H_2O$, ~0.14 M) was dissolved in ethanol or acetone (80 mL) under constant stirring. Subsequently, the basic environment (KOH, ~2 M) was slowly added to the solution until pH=10 was reached. The resulting solution was heat treated at 100°C for 8 min with a heating rate of 10°C/min, according to previous results reported by our group[37] into a sealed Teflon autoclave and placed in an adapted microwave (2.45 GHz, maximum power of 800 W), then cooled until room x temperature naturally. The CeO_2 NCs were centrifuged and washed with deionized water three times until pH = 7 and then dried in an oven at 100°C for 48 hours.

2.2 Nanocrystal characterization

2.2.1. Structural and morphology characterization

The crystal structure of the samples was characterized using X-ray powder diffraction (PXRD). Diffractograms were collected on a Rigaku-DMax (model 2500PC, Japan) using Cu-K_α radiation (λ=1.5406 Å) over a 15°-85° 2θ range at 0.02°/min, using a collection time of 8 s/point and 2.0 mm receiving slit. The *Rietveld* method[53] was used to refine the crystal structure of the powders on Topas V5 in its academic version[54]. Specific surface area (BET) measurements were performed on a Micromeritics ASAP 2010 equipment with 0.1 g/sample under a nitrogen atmosphere at 77 K. To eliminate humidity, samples were dried at 350°C for 24 hours before analysis. Raman spectroscopy was carried out on a T64000 spectrometer (Horiba Jobin-Yvon, Japan) using an argon-ion laser with λ=633 nm (7 mW) over the 25–1200 cm^{-1} range. Chemical surface analysis was performed on all samples using X-ray photoelectron spectroscopy (XPS) using a conventional XPS spectrometer (ScientaOmicron ESCA+) consisting of a high-performance hemispheric analyzer (EAC2000) and an *Al* K_α (hv=1486.6 eV) monochromatic

excitation source. Analysis was performed under ultra-high vacuum (UHV) operating pressure ~ 10^{-9} Pa. XPS high-resolution spectra were recorded at constant pass energy (20 eV; 0.05 eV step size) using a charge neutralizer (CN10) to eliminate surface charging effects. XPS peak fitting was performed on CASA XPS software. The morphology was examined using a Phillips FEI CM 120 transmission electron microscope operating at 200 kV The images were taken at room temperature in a Phillips FEI CM 120 microscope after the samples were dispersed in ethanol, deposited onto 300 mesh copper grids, and dried.

2.2.2. Optical characterization.

Ultraviolet-visible (UV-vis) spectra were obtained using a Varian spectrophotometer (model Cary 5G, USA) in diffuse reflectance mode. To estimate the bandgap energy, the UV-Vis data were converted into Tauc plots via the Kubelka-Munk function, considering indirect type allowed transitions for the samples (n=2). The y-axis corresponds to the transformed *Kubelka-Munk* function ($[F(R_\infty)hv]^{1/2}$) and the x-axis to the photon energy. The bandgap energy corresponds to the interception point between the extrapolation of the linear fit of the curves and the x-axis. Fourier transformed infrared spectroscopy (FTIR) spectra were obtained using a Bruker (model Equinox-55) in transmittance mode using an Attenuated Total Reflection (ATR) mode sample holder. PL emission data were measured at room temperature on a monospec27 Jarrel-Ash monochromator with a Hamamatsu R446 photomultiplier operating with a coherent Innova Argon-ion laser (λ_{exc}=350.7 nm; 2.57 eV, 200 mW). Each spectrum was appropriately deconvoluted, and the associated points on the chromaticity diagram (CIE 1931) were obtained based on the PL spectrum for each sample using Origin® 2019 software.

Photocatalytic experiments were performed using 15 mg of the photocatalyst (0.3 g L^{-1}) which was added to 50 mL of standardized rhodamine-B (RhB) dye (10^{-5} mol L^{-1} solution). Before irradiation, the suspension was magnetically stirred for 45 min in the dark at room temperature to achieve the adsorption/desorption equilibrium. After that, the suspension was illuminated by six lamps (lamp λ_{max}=254 nm, PHILIPS TL-D, 15 W) (~9.55 mW/cm^2 at the center of the reaction vessel) with air bubbling and constant stirring. In situ capture photocatalytic experiments using scavengers were conducted to capture the active species in the semiconductor and predict the degradation mechanism. The compounds used as scavengers were e^- (silver nitrate), h^+ (ammonium oxalate), •OH (tert-butyl alcohol), and $•O^{2-}$ (p-benzoquinone). Aliquots were withdrawn at certain times, centrifuged, and analyzed via absorption spectroscopy using

aspectrophotometer (Femto Cirrus 80PR). The photocatalytic efficiency was calculated according to the percentage of absorbance of the dye solution, using Eq. 1:

$$Degradation\ \% = \frac{C_0 - C_t}{C_0} \quad (1)$$

where C_0 and C_t indicate the concentration of dye at time t = 0 and t, respectively.

2.2.3. First-principle calculations

Different surfaces were modeled using unreconstructed (truncated bulk) slab models with calculated equilibrium geometries[55–57]. (001), (110), and (111) CeO_2 surfaces were simulated considering symmetrical slabs with respect to the mirror plane. The surface energy (E_{surf}) was calculated using Eq. 2:

$$E_{surf} = \frac{(E_{slab} - nE_{bulk})}{2A} \quad (2)$$

where represents E_{slab} is the total slab surface energy per molecular unit, n the number of molecular units, E_{bulk} the bulk total energy of the bulk, and A is the surface area.

The *Wulff* construction, in particular when linked to first-principle calculations, is a powerful tool for predicting the possible morphologies of crystalline materials[49,58–62].*Wulff* constructions can be used to calculate the equilibrium shape of a crystal considering total surface free energy minimization at a fixed volume, based on the relation between E_{surf} of a specific crystallographic plane and its distance from the crystallite center in the normal direction[63]. Using Visualization for Electronic and Structural Analysis (VESTA) to obtain the morphology of the CeO_2 NCs[64], we prepared a map of all available CeO_2 NCs morphologies by changing the relative surface energy values for each facet, as well as the pathways linking the different morphologies, including cubic, truncated cubic, octahedral, truncated octahedral, rhombic dodecahedral, and rhombic cuboctahedral.

3. Results and discussions

3.1. Structural characterization.

Fig. 1(a-b) shows PXRD patterns obtained for the CeO_2 NCs synthesized using MAS with acetone (Fig. 1a) and ethanol (Fig. 1b) as solvents. On both samples, all the diffraction peaks belong to the CeO_2 phase (ICSD #29046) with fluorite structure and *Fm-3m* space group without any apparent secondary-phase peaks[65]. *Rietveld* parameters (χ^2, R_{exp}, R_{wp}, R_p) shown in Table 1

indicate a coherent PXRD data fitting[66]. The lattice volume (Table 1) has not significantly changed for the samples synthesized using acetone compared to ethanol. On samples synthesized using ethanol, (111), (200), and (220) peak intensities increase, indicating that these crystallographic planes are favored during crystallization due to the higher dielectric loss of ethanol (*tanδ*~1.0), which is more efficient converting microwaves into thermal energy, heating the solution faster in comparison to acetone (*tanδ*<0.1)[67,68]. Additionally, crystallite size determined by *Rietveld* analysis was found to be 14.2 and 20.7 nm for samples synthesized using acetone and ethanol, respectively. Deviations in crystallite size can be caused by strain and crystal lattice imperfections, which affect peak position as well as peak asymmetry, broadening, and shape effects, as shown by PXRD data. FT-IR analyzes were also performed, corroborating the PXRD results (see Fig. S1 in *Supporting Information*). Additionally, the sample synthesized in acetone exhibited a slight increase in the full width at half maximum (FWHM) (≈0.69) compared to the sample synthesized in ethanol (≈0.64), indicating higher long-range disorder in acetone[69].

<INSERT **FIGURE 1**>

Figure 1 - Rietveld analysis for the CeO_2 samples synthesized by MAS using (a) acetone and (b) ethanol. (c) Raman spectra for the CeO_2 samples synthesized via MAS using acetone and ethanol.

Table 1 - Structural and Rietveld parameters, specific surface area Brunauer–Emmett–Teller (BET) and adsorption pore diameter values, and gas sensing response and recovery time for the CeO_2 samples synthesized by MAS using acetone and ethanol.

<INSERT **TABLE 1**>

To investigate how the solvent influences physical properties of the CeO_2 NCs, specific surface area measurements were performed using the *Brunauer–Emmett–Teller* (BET) method, whose results are shown in Table 1. Samples synthesized in acetone revealed smaller crystallites/ higher specific surface area. This may lead to high reactant concentration, generating larger agglomeration of particles. Crystal growth is a function of: (1) induction time, during which the reaction slowly generates growth solid unit; (2) nucleation, when concentration in the solution builds up until a critical supersaturation is reached; and (3) particle growth, which proceeds until the reaction stops due to the solution having reached equilibrium[36].

Fig. 1 (d) displays Raman spectra of the samples. Mode F_2g (~464 cm^{-1}) is characteristic of the cubic fluorite structure in CeO_2[70], and may be associated with symmetrical Ce–O bond stretching/breathing vibrations in a coordination polyhedral in which eight O^{2-} ions form a cube around a central Ce^{4+} ion[71]. [CeO_8] clusters are extremely sensitive to any vibrations in the O^{2-} sublattice and their positions[39]. Hence, a relatively weak vibrational mode at ~600 cm^{-1}, commonly referred to as d-mode (or defect induced mode) are related to short-range structural defects. In this case, the formation of oxygen vacancies can be considered, and ascribed to the intrinsic reduction of Ce^{4+} ions into Ce^{3+}, is driven on the samples synthesized in acetone[20,41]. At ~1042 cm^{-1} occurs a second-order Raman mode, which has been associated with the presence of the Ce^{3+} ions within the structure, but also to peroxide and O^{2-} ions[39,40,72,73]. Chen *et al.*[74] reported $Ce^{3+}\rightarrow Ce^{4+}$ transition effects and, hence, lower oxygen vacancy density, associated with the formation of Ce-OH and Ce-O bonds on CeO_2 nano-needles synthesized via two-stage non-isothermal precipitation, which explains why mode at ~600 and 1042 cm^{-1} fade on the sample synthesized in ethanol. The work of Zhang *et al.*[68] further supports this hypothesis. Additionally, oxygen vacancies can generate hole-trapping centers as a result of the formation of $[CeO_8]_d^x$ or $[CeO_8]_d^x/[CeO_7.V_O^x]$ complex clusters within the CeO_2 structure [41]. Mode width/position are extremely sensitive to disorder at the sites occupied by oxygen ions in the crystalline oxide lattice. Additionally, sample synthesized using ethanol display a more intense F_2g mode compared to the sample synthesized in acetone, indicating the higher crystallite size. This result is in agreement with the *Rietveld* analysis shown in Table 1. Therefore, the increase in intensity observed on Raman spectrum for the sample synthesized in ethanol can be associated with preferential growth orientation[75,76], as perceived by the higher intensity (111) relative intensity. Furthermore, the full width at half maximum (FWHM) estimated for each of the samples, suggests higher short-range disorder on the sample synthesized in acetone (≈22.26), compared to the sample synthesized in ethanol (≈20.02), which can be a result of an increase in the density of oxygen vacancies within the crystal lattice. This result is in agreement with associated with the kinetics of synthesis conditions and also the intrinsic lattice structural order as was confirmed by the PXRD/Rietveld refinement.

Figure 2 (a-b) displays the O *1s* XPS spectra. For both samples the oxygen, the peak was deconvolved into three components, the one around 529 eV ($O_{lattice}$) has been attributed to Ce-O bonds within the CeO_2 lattice; at ≈531 eV ($O_{vacancy}$) the peak can be ascribed to oxygen vacancies,

as well as to carbon containing molecules attached to the surface of the material, hydroxyl groups and adsorbed oxygen species[77]. Finally, at ≈533 eV (O_C) has been attributed to the O-C bonds. The intensity of the component associated with lattice oxygen decreases for the sample synthesized in acetone sample, whereas the component associated with oxygen vacancies greater increases its intensity. Torrente-Murciano *et al.*[77] reported on the possibility to estimate oxygen vacancies in the samples, which can be derived from the $O_{vacancy}/O_{lattice}$ ratio. Using this relationship, the values found were 0.57 and 1.27 for the ethanol and acetone samples, respectively, suggesting a greater oxygen vacancy density on the surface of the sample synthesized in acetone compared to the ones synthesized in ethanol, corroborating the Raman data. Ce *3d* XPS spectra obtained for the samples synthesized in acetone and ethanol are provide in the supplementary information (Figure S2). Although it was not possible to quantify Ce^{3+}/Ce^{4+} content in the samples, qualitative analysis of Ce *3d* XPS spectra suggests a lower Ce^{4+} content in the samples synthesized in acetone, which may be associated with a higher oxygen vacancy density in agreement with the analysis regarding O *1s* levels..

<INSERT **FIGURE 2**>

Figure 2 – O *1s* XPS peak fitting for the samples synthesized in acetone and ethanol.

Fig. 3 shows transmission electron microscopy (TEM/ HRTEM) micrograph images for the samples. TEM in Fig 3(a) reveals the formation of nanorods and nanoparticles for the sample synthesized in acetone, while samples synthesized in ethanol only exhibit octahedral-like nanoparticles (Fig 3d). The nanorods present in the samples synthesized in acetone showed an average thickness of 12 nm with over 100 nm in length. These nanoparticles presented (100), (110) and (111) planes (Fig. 3b-c), which are the most commonly exposed planes in ceria samples[78,79]. Similarly, to the samples synthesized in acetone, the ethanol samples exhibit the (110) and (111) planes were (Fig. 3e-f). Anisotropic growth of the CeO_2 NCs may be a result of the formation of complexes between cerium hydroxide and ethanol molecules, resulting in octahedral-like shaped nanoparticles (Fig. 3e-f)[68]. Nucleation and crystal growth of nanostructures under hydrothermal/solvothermal conditions are governed by multiple parameters, such as temperature, time, environment, solvent type, precursor type, precursor concentration, pH, vessel size, solution volume, pressure, etc.[80]. Regarding the solvothermal synthesis, three parameters associated with the solvent are known to influence the crystal growth, which are: precursor solubility in a chosen

solvent, solvent polarity, and their characteristic vapor pressure[81]. For instance, Mishra *et al*.[31] synthesized CuO nanostructures via MAS using a water-ethylene glycol mixture as solvent. The authors obtained 3D CuO nanoarchitectures composed of either rods or flakes as building blocks, which they associated to the precursor type (copper acetate and copper nitrate) and to the water-ethylene glycol mixture vapor pressure. Analogously, Xu *et al*.[81] used water, ethanol, acetone, toluene, decane, and THF to synthesize ZnO nanostructures with multiple shapes, such as sphere, rod, cauliflower-like, hourglass-like, and conical hexagon. The results obtained in this work corroborate the work of Zhang *et al*.[68]. Therefore, we can infer that solvents with different polarities and saturated vapor pressures affect the morphology of samples synthesized under solvothermal treatment because they will have different chelating effects with the metal cations leading to different crystal growth habits. That will lead to initial nucleation, agglomeration, and preferred orientation of the crystals.

<INSERT **FIGURE 3**>

Figure 3 – TEM and HRTEM micrograph images for the CeO_2 samples synthesized via MAS in (a-c) acetone and (d-f) ethanol.

3.2. First-principle calculations

Fig. 4 shows *Wulff* constructions for the investigated surfaces (100), (110), and (111) of CeO_2 generated at different thermodynamic conditions. *Wulff* constructions are associated with exposed facet stability and can be employed to explain morphologies. Morphology changes with the ratio associated E_{surf} values of each surface, where the rate of the individual surface is dependent on the different values of E_{surf}. Based on thermodynamics, final morphology is defined by stability of each of the different surfaces interacting with ions on the surface (*e.g.,* O_2, etc.)[37]. E_{surf} indicates that surfaces (111) minimize surface energy – is the most stable. Careful inspection of the *Wulff* constructions exhibits octahedron-shaped particles composed of different percentages of surfaces (100), (111), and (110). Crystal shape (I) is dominated by surface (111) followed by surface (110). When the oxygen chemical potential is reduced, surface (111) percentage is gradually replaced by surfaces (110) and (100), respectively[82,83]. Additionally, the actual surface energy on metal oxides depends on other factors such as bond contractions and surface electronic structure[83]. To obtain the crystal shape (II), there is an area reduction of the surface (111) and the relative increase of the crystal coverage by the surface (100), resulting from

the decrease of E_{surf} (100). The theoretical simulations represented in the Wulff constructions are corroborated by TEM micrograph images, indicating that the exposed planes predicted in theory are indeed experimentally reproduced. In addition, the octahedral shape of the nanoparticles obtained by synthesis in ethanol is associated, especially with the crystal shape (III). Thus, using ethanol as a solvent may favor the decrease of E_{surf} (110) and (111).

<INSERT **FIGURE 4**>

Figure 4 - Crystallographic structure based on *Wulff* constructions for CeO_2 with crystal planes (111), (110) and (100).

3.3. Optical characterization

Fig. 5 shows EPR curves for each of the samples. Broad resonance at B_0=3380 G may be associated with $Ce^{3+}_{(CeO7)}$-$O_{2(surface)}$ interactions, which creates an oxygen-active surface. Samples synthesized in acetone show higher B_0 intensity, indicating that synthesis in acetone may produce a higher oxygen vacancy density CeO_2 structure, proving the presence of paramagnetic Ce^{3+} species ([Xe] $4f^1\ 5d^0$)[43]. This result is in accordance with the bandgap value obtained for each sample, suggesting the formation of a larger number of defects on samples synthesized in acetone (E_{gap}=2.52 eV), whereas a more organized crystal may be associated with the sample prepared in ethanol (E_{gap}=2.81 eV). Additionally, EPR analysis confirms the Raman and XPS results. Samples synthesized in ethanol, g-value shifts slightly towards smaller values (larger B_0), which can be associated with variations in surface electron-coupling properties. The signal of B≈3400 G may also be associated with the presence of Ce^{3+} ions on the CeO_2 surface.

<INSERT **FIGURE 5**>

Figure 5 - EPR spectra for CeO_2 samples synthesized via MAS in ethanol and acetone.

Fig. 6(a-b) show PL emission spectra obtained at room temperature for CeO_2 NCs synthesized in acetone and ethanol, respectively. NCs synthesized in acetone (Fig. 6a) show greater contribution of emission peaks in the blue region (~450 nm), which may be associated with oxygen-related defects related to F center formation as a result of higher Ce^{3+} content and is characterized by $4f^1 \leftrightarrow 5d^1$ optical transitions, originating shallow-level defects within the CeO_2 lattice compared to the ones synthesized in ethanol (Fig. 6b) as confirmed by Raman and XPS

spectroscopies, as well as EPR. As Ce^{3+} concentration increases, so does the $V_O^{\bullet}$ density within the crystal lattice as shown in Eq. 4:

$$CeO_8 + 1e^- \rightarrow CeO_7.V_O^{\bullet} \quad (4)$$

<INSERT **FIGURE 6**>

Figure 6 – PL spectrum deconvolution for the CeO_2 samples synthesized via MAS in (a) acetone and (b) ethanol. The (c) proposed electronic structure model/emission mechanism, and (d) chromaticity diagram (CIE 1931) for the CeO_2 samples.

Thus, a stronger orange-red emission peak (~595 nm) in the NCs synthesized in ethanol suggest that oxygen vacancies may originate from deep-level defects within the optical bandgap region. Additionally, superficial oxygen-containing functional groups both on NCs synthesized in acetone and ethanol can lead to electronic transitions between O *2p* states and higher energy levels, generating self-trapped excitons[84].

The CeO_2 cubic structure is characterized by oxygen ions, which are not closely packed; hence, ceria forms many oxygen vacancies. Several authors have associated CeO_2 emissions to *4f→VB* (valence band) transitions, producing a violet-blue emission (~422 nm)[84,85] strongly influenced by photoreduction (nephelauxetic effect) that leads to the presence of Ce^{4+} and Ce^{3+} ions simultaneously within the CeO_2 structure at the expense of oxygen vacancy ($V_O^{\bullet}$) formation. Trapping of electron pair in $V_O^{\bullet}$ cavities ($V_O^{\bullet} + e^- \rightarrow V_O^-$) establishes F centers within the optical bandgap region, below *4f* states. Both samples show typical CeO_2 broadband emission spectrum dominated by Ce^{3+}-related emissions characterized by $4f^1 \leftrightarrow 5d^1$ optical transitions, which may be displaced according to the crystalline field, whereas Ce^{4+} does not show optical activity due to its [Xe] electronic configuration. CeO_2 morphology and chemical environment strongly influence the Ce^{3+} ground ([Xe]$4f^1$) and excited ([Xe]$5d^1$) state configurations[86–88].

Theoretical-experimental data was used to propose a practical model to explain the MAS synthesis-solvent (acetone/ethanol) role on the electronic structure, and PL response of CeO_2 NCs (Fig 6c). Fig. 6(b) shows the chromaticity diagram (CIE – *Commission internationale de l'eclairage* 1931), which evidences the different emissions for samples synthesized in acetone and ethanol. The CIE representation also gives information on the correlated color temperature (CCT) of the samples and can be associated with final practical application of fluorescent lights and LEDs. For common LED materials the CCT (in Kelvin) the emitted light can vary over a wide range

(2700–6500K). Ethanol produces PL emission in the "ultra-warm" white region (3000K) characteristic of incandescent light bulb emissions, whereas acetone synthesized samples "are on" the "cool white" zone (4660 K) of the CIE diagram, relate to daylight or an RGB monitor reference white point. Warm light region appears less bright to humans and are generally associated with resting areas (acetone, ~3000 K), whereas samples emitting in cooler regions are indicated for working environments (ethanol, 4660 K)[89].

Fig. 7(a-c) show photodegradation experiments using RhB dye solution as a model molecule to evaluate photocatalytic activity. Photocatalysis may be described as a three-step process: (I) target molecules are adsorbed on the surface of the catalyst; (II) radiation is absorbed by the catalyst producing photogenerated pairs (e^--h^+); and (III) redox reactions between molecules of the medium and the photogenerated pairs occur[90].

<INSERT **FIGURE 7**>

Figure 7 – (a) CeO_2 samples photocatalytic behavior; Photocatalysis results with kinetics adjustments using the (b) pseudo-second order model, and (c) pseudo-first order model, respectively. (d) Scavengers test for the CeO_2 samples, and (e) possible ROS generation mechanism.

Taking into consideration the adsorption of the samples, one can observe that CeO_2 NCs synthesized in acetone adsorbs ~18% of the RhB in the solution, while the CeO_2 NCs synthesized in ethanol adsorbs ~9% (Figure 7a). The adsorptive process is superficial and CeO_2 NCs showed synthesized in acetone higher have larger surface area. The photocatalytic behavior of the samples synthesized in acetone proved much superior to that of samples synthesized in ethanol, degrading 80% of RhB in 240 min. The samples synthesized in ethanol showed superior performance to that observed for photolysis, degrading 24% RhB in 240 min. This highlights an impressive feature, which is that the solvent used in the synthesis can significantly alter the structural, electronic and photocatalytic properties of CeO_2. As evidenced by the *Wulff* construction and TEM micrograph images, surface (100) prevails in the morphology of nanoparticles synthesized in ethanol, causing a significant decrease in its photocatalytic efficiency. RhB photocatalytic decomposition may be attributed to different kinetic models, such as the pseudo-first order one, which is based on a simplified Langmuir-Hinshelwood model (Eq. 5)[91], or the pseudo-second order one (Eq. 6)[92]:

$$\ln(C_n/C_0) = -kt \quad (5)$$

$$1/C_n - 1/C_0 = kt \quad (6)$$

where the kinetic rate constant (k) is determined from a linear fit to the data, t is the time, C_0 the initial concentration and C_n the concentration variation.

The photocatalytic process of the CeO_2 NCs shows a much higher goodness of fit (R^2 values) using the pseudo-second order kinetic reaction equation as shown in Fig. 7(b). Based on these results, we confirmed that it was inappropriate to describe RhB photodegradation reaction as a pseudo-first order kinetic reaction (Fig. 7c), which indicates that the reaction rate is proportional to the reagent concentration[92]. k values obtained for the pseudo-second order fit were 5.78×10^{-3} and 6.3×10^{-4} $L.mol^{-1}.min^{-1}$ for CeO_2 NCs synthesized in acetone and in ethanol, respectively. The improvement in photocatalytic activity of the sample synthesized in acetone may be due to several factors, such as the increase in long- and short-range disorder evidenced by a decrease in ordering within the CeO_2 crystal structure as evidenced by PXRD and Raman measurements. This disorder ends up generating defects in the forbidden region of the bandgap, increasing the number of shallow-level defects in CeO_2 (see PL results), causing the E_{gap} value to decrease. This reduction facilitates the absorption of light by CeO_2, thus, increasing photocatalysis efficiency by increasing the concentration of photogenerated pairs and decreasing their recombination processes.

The use of CeO_2-based materials for the degradation of organic dyes has been reported by several researchers. A comparison showing the photocatalytic response of different CeO_2-based materials and its parameters is shown in Table 2. Our work shows promising results compared to what has been reported by Su *et al.*[93] (16.99%), Tuyen *et al.*[94] (~5%), Yu *et al.*[95] (26.8%), Mandal *et al.*[96] (63%), and Wangkawong *et al.*[97] (12%) regarding the degradation of RhB by pure CeO_2. On the other hand, the comparison presented in Table 2 shows that the photocatalytic response can be significantly enhanced by the formation of heterostructures.

<INSERT **TABLE 2>**

Fig. 7(d) shows the results of scavenger tests performed for the CeO_2 NCs used to unveil the RhB photodegradation process. To investigate its mechanism selective scavengers of different reactive species e^- (silver nitrate), h^+ (ammonium oxalate), •OH (tert-butyl alcohol) and $\bullet O_2^-$ (p-benzoquinone) where added to the RhB solutions[98–101]. While no significant changes were observed on the samples synthesized in ethanol since their photocatalytic efficiency is very close

to actual photolysis, on the sample synthesized in acetone, a reduction for all scavengers can be observed, especially the $\bullet O_2^-$ radical. Hence, we know that in the degradation process, all reactive species participate in breaking down the RhB molecule, and there is a greater contribution of $\bullet O_2^-$ radicals. In Fig. 7(e), CeO_2 clusters with oxygen vacancies (V_O) are represented by the general formula [$CeO_7.V_O$]. V_O present in the clusters can become $V_O^{\bullet}$ and $V_O^{\bullet\bullet}$ depending on how photogenerated e^--h^+ pairs shift on the CeO_2 surface by cluster-cluster charge transfer (a and b in Fig. 7e; steps a-b). According to Tello *et al.*[102], $V_O^{\bullet}/V_O^{\bullet\bullet}$ formation in the clusters favors the processes that lead to H_2O oxidation/O_2 reduction (Figure 7e; steps d-e), resulting in the formation of $\bullet OH$ and $\bullet O_2^-$ radicals. After the redox processes, the clusters regenerate, continuing the oxidation processes (Fig. 7; steps c-e). The $\bullet OOH$ radical is generated by the reaction of a proton - $\bullet H$ - with a superoxide radical - $\bullet O_2^-$ - (Figure 7e; step f)[103].

4. Conclusions

In this work, MAS synthesis-solvent influence on crystal structure, morphology, PL, and photocatalytic properties of CeO_2 NCs was investigated using a theoretical-experimental approach. PXRD, Raman, and FT-IR results show that CeO_2 NCs synthesized in ethanol or acetone crystallized in the fluorite cubic structure, free of secondary-phases and contaminants. The solvent used in the synthesis (ethanol/acetone) results in changes to the density of defects within the CeO_2 structure and the morphology of the nanocrystals, altering their photocatalytic responses. Using *Wulff* constructions, a complete map of available morphologies was built, and a theoretical-experimental match was obtained for the samples synthesized in ethanol, which exhibited octahedral nanoparticles. CeO_2 NCs synthesized in acetone showed superior photocatalytic response than that of CeO_2 NCs synthesized in ethanol, which may be a result of an increase in long-/short-range disorder within the CeO_2 structure, causing the E_{gap} value to decrease facilitating light absorption by CeO_2, as well as higher surface area due to the presence of sphere-like nanoparticles in the samples synthesized in ethanol as opposed to a combination of nanorods/nanoparticles in the samples synthesized in acetone. These results may also be associated with NCs synthesized in acetone show greater contribution of emission peaks in the blue region (~450 nm), which may be associated with higher Ce^{3+} concentration, originating shallow-level defects within the CeO_2 lattice while for the samples synthesized in ethanol a strong orange-red emission (~595 nm) suggests that oxygen vacancies may originate from deep-level defects within

the optical bandgap region. Our results showed an impressive feature, that solvent used in the synthesis can significantly alter the structural, electronic, and photocatalytic properties of CeO_2 NCs, and a mechanism of enhanced photocatalytic activity has been proposed suggesting that the higher photocatalytic response in the samples synthesized in acetone may be related to lower e'—$h^{\bullet}$ pair recombination, facilitated by the generation of •OH and $\bullet O_2^-$ radicals, whereas on the samples synthesized in ethanol surface (100) stabilization may lead to low photocatalytic activity.

Author information

Corresponding Author

Henrique Moreno – São Paulo State University (UNESP), School of Engineering of Guaratingueta, Av. Dr. Ariberto Pereira da Cunha 333, Portal das Colinas, 12516-410, Guaratinguetá, São Paulo, Brazil. *hpiccolimoreno@gmail.com

Authors

Giulio. L. Domingues – São Paulo State University (UNESP), School of Engineering of Guaratingueta, Av. Dr. Ariberto Pereira da Cunha 333, Portal das Colinas, 12516-410, Guaratinguetá, São Paulo, Brazil.

Marcelo Assis – Department of Analytical and Physical Chemistry, University Jaume I (UJI), Av. Vicent Sos Baynat s/n, Castelló, 12071, Spain.

Pedro P. Ortega – São Paulo State University (UNESP), School of Engineering of Guaratingueta, Av. Dr. Ariberto Pereira da Cunha 333, Portal das Colinas, 12516-410, Guaratinguetá, São Paulo, Brazil.

Valmor R. Mastelaro – São Carlos Institute of Physics, University of São Paulo, 13566-590 São Carlos, Brazil

Miguel A. Ramirez – São Paulo State University (UNESP), School of Engineering of Guaratingueta, Av. Dr. Ariberto Pereira da Cunha 333, Portal das Colinas, 12516-410, Guaratinguetá, São Paulo, Brazil.

Alexandre Z. Simões – São Paulo State University (UNESP), School of Engineering of Guaratingueta, Av. Dr. Ariberto Pereira da Cunha 333, Portal das Colinas, 12516-410, Guaratinguetá, São Paulo, Brazil.

The manuscript was written through contributions of all authors. All authors have given approval to the final version of the manuscript.

Notes

The authors declare no competing financial interest.

Supporting Information

FTIR and UV-vis data/bandgap energy (E_{gap}) values for each of the samples (PDF).

5. Acknowledgment

The authors appreciate the support of the Brazilian research financing institution: FAPESP CDMF grants n.: 2013/07296-2 and n.: 2018/18236-4, Elson Longo for *Wullf* diagrams, and U. Wiedwald for the EPR and PL measurements. M.A. was supported by the Margarita Salas postdoctoral contract MGS/2021/21 (UP2021-021) financed by the European Union-Next Generation EU.

6. References

(1) Yang, H. G.; Sun, C. H.; Qiao, S. Z.; Zou, J.; Liu, G.; Smith, S. C.; Cheng, H. M.; Lu, G. Q. Anatase TiO2 Single Crystals with a Large Percentage of Reactive Facets. *Nature* **2008**, *453* (7195), 638–641. https://doi.org/10.1038/nature06964.

(2) Polarz, S. Shape Matters: Anisotropy of the Morphology of Inorganic Colloidal Particles - Synthesis and Function. *Adv Funct Mater* **2011**, *21* (17), 3214–3230. https://doi.org/10.1002/adfm.201101205.

(3) Lai, F.; Chen, Y.; Guo, H. Surface Energies of Non-Centrosymmetric Nanocrystals by the Inverse Wulff Construction Method. *Physical Chemistry Chemical Physics* **2019**, *21* (30), 16486–16496. https://doi.org/10.1039/c9cp01975h.

(4) Lai, F.; Chen, Y.; Guo, H. Inverse Wulff Construction for Surface Energies of Coexisting and Missing Surfaces of Crystal Particles. *J Cryst Growth* **2019**, *508*, 1–7. https://doi.org/10.1016/j.jcrysgro.2018.12.006.

(5) Wang, Z.; Liu, L.; Du, Q.; Tang, R.; Ai, J.; Chen, Y. Enhanced Microwave Dielectric Properties of CeO2-TiO2 Ceramics by Adding Al2O3 Microstrip Antenna Application. *Ceram Int* **2022**, *48*, 14378–14385.

(6) Jaidka, S.; Khan, S.; Singh, K. Na2O Doped CeO2 and Their Structural, Optical, Conducting and Dielectric Properties. *Physica B Condens Matter* **2018**, *550*, 189–198. https://doi.org/10.1016/j.physb.2018.08.036.

(7) Rocha, L. S. R.; Amoresi, R. A. C.; Moreno, H.; Ramirez, M. A.; Ponce, M. A.; Foschini, C. R.; Longo, E.; Simões, A. Z. Novel Approaches of Nanoceria with Magnetic, Photoluminescent, and Gas-Sensing Properties. *ACS Omega* **2020**, *5* (25), 14879–14889. https://doi.org/10.1021/ACSOMEGA.9B04250/ASSET/IMAGES/LARGE/AO9B04250_0007.JPEG.

(8) Ortega, P. P.; Rocha, L. S. R.; Cortés, J. A.; Ramirez, M. A.; Buono, C.; Ponce, M. A.; Simões, A. Z. Towards Carbon Monoxide Sensors Based on Europium Doped Cerium Dioxide. *Appl Surf Sci* **2019**, *464* (June 2018), 692–699. https://doi.org/10.1016/j.apsusc.2018.09.142.

(9) Balaguer, M.; Solís, C.; Escolástico, S.; Garcia-Fayos, J.; Serra, J. M. Evaluation of Er Doped CeO2-δ as Oxygen Transport Membrane. *Membranes (Basel)* **2022**, *12* (2), 172. https://doi.org/10.3390/MEMBRANES12020172/S1.

(10) Regmi, C.; Ashtiani, S.; Sofer, Z.; Hrdlička, Z.; Průša, F.; Vopička, O.; Friess, K. CeO2-Blended Cellulose Triacetate Mixed-Matrix Membranes for Selective CO2 Separation. *Membranes (Basel)* **2021**, *11* (8), 632. https://doi.org/10.3390/MEMBRANES11080632/S1.

(11) Akhlaghinia, B.; H., Ebrahimabadi.; Goharshadi, E. K.; Samiee, S.; Rezazadeh, S. Ceria Nanoparticles as an Efficient Catalyst for Oxidation of Benzylic C-H Bonds. *Jounral of Molecular Catalysis A: Chemical* **2012**, *357*, 67–72.

(12) Miller, H. A.; Bellini, M.; Dekel, D. R.; Vizza, F. Recent Developments in Pd-CeO2 Nano-Composite Electrocatalysts for Anodic Reactions in Anion Exchange Membrane Fuel Cells. *Electrochem commun* **2022**, *135*, 107219. https://doi.org/10.1016/J.ELECOM.2022.107219.

(13) Choi, J.; Yeon, J. H.; Yook, S. H.; Shin, S.; Kim, J. Y.; Choi, M.; Jang, S. Multifunctional Nafion/CeO2Dendritic Structures for Enhanced Durability and Performance of Polymer Electrolyte Membrane Fuel Cells. *ACS Appl Mater Interfaces* **2021**, *13* (1), 806–815. https://doi.org/10.1021/ACSAMI.0C21176/ASSET/IMAGES/MEDIUM/AM0C21176_M007.GIF.

(14) Yuk, S.; Jung, J.; Song, K. Y.; Wook Lee, D.; Lee, D. H.; Choi, S.; Doo, G.; Hyun, J.; Kwen, J.; Young Kim, J.; Kim, H. T. Addressing the Detrimental Effect of CeO2 Radical Scavenger on the Durability of Polymer Electrolyte Membrane Fuel Cells. *Chemical Engineering Journal* **2023**, *452*, 139061. https://doi.org/10.1016/J.CEJ.2022.139061.

(15) Wang, L.; Xu, G.; Liu, C.; Hou, H.; Tan, S. Surface-Modified CeO2 Coating with Excellent Thermal Shock Resistance Performance and Low Infrared Emissivity at High-Temperature. *Surf Coat Technol* **2019**, *357*, 559–566. https://doi.org/10.1016/J.SURFCOAT.2018.10.058.

(16) Wu, Y.; Jiang, F.; Qiang, Y.; Zhao, W. Synthesizing a Novel Fluorinated Reduced Graphene Oxide-CeO2 Hybrid Nanofiller to Achieve Highly Corrosion Protection for Waterborne Epoxy Coatings. *Carbon N Y* **2021**, *176*, 39–51. https://doi.org/10.1016/J.CARBON.2021.01.135.

(17) Yanan, L.; Ronglu, S.; Wei, N.; Tiangang, Z.; Yiwen, L. Effects of CeO2 on Microstructure and Properties of TiC/Ti2Ni Reinforced Ti-Based Laser Cladding Composite Coatings. *Opt Lasers Eng* **2019**, *120*, 84–94. https://doi.org/10.1016/J.OPTLASENG.2019.03.001.

(18) Fu, C.; Sun, Y.; Huang, C.; Wang, F.; Li, N.; Zhang, L.; Ge, S.; Yu, J. Ultrasensitive Sandwich-like Electrochemical Biosensor Based on Core-Shell Pt@CeO2 as Signal Tags and Double Molecular Recognition for Cerebral Dopamine Detection. *Talanta* **2021**, *223*, 121719. https://doi.org/10.1016/J.TALANTA.2020.121719.

(19) Shcherbakov, A. B.; Reukov, V. v.; Yakimansky, A. v.; Krasnopeeva, E. L.; Ivanova, O. S.; Popov, A. L.; Ivanov, V. K. CeO2 Nanoparticle-Containing Polymers for Biomedical Applications: A Review. *Polymers 2021, Vol. 13, Page 924* **2021**, *13* (6), 924. https://doi.org/10.3390/POLYM13060924.

(20) Ortega, P. P.; Hangai, B.; Moreno, H.; Rocha, L. S. R.; Ramírez, M. A.; Ponce, M. A.; Longo, E.; Simões, A. Z. Tuning Structural, Optical, and Gas Sensing Properties of Ceria-Based Materials by Rare-Earth Doping. *J Alloys Compd* **2021**, *888*, 161517.

(21) Singh, A.; Saini, R.; Kumar, P.; Kandasami, A. Tailoring of Defects Dependent Magnetic Properties of Swift Heavy Ion Irradiated CeO2 for Spintronics Application. *J Appl Phys* **2022**, *132* (12), 125901. https://doi.org/10.1063/5.0088882.

(22) Shibeshi, P. T.; Parajuli, D.; Murali, N. Study of Fe-Doped and Glucose-Capped CeO2 Nanoparticles Synthesized by Co-Precipitation Method. *Chem Phys* **2022**, *561*, 111617. https://doi.org/10.1016/J.CHEMPHYS.2022.111617.

(23) Gonzaga, L. A.; Santana, V. T.; Bernardi, M. I. B.; Hrubý, J.; Neugebauer, P.; Mesquita, A. CeO2 and CeO2:Pr Nanocrystalline Powders Prepared by the Polymeric Precursor Method: Yellow and Red Pigments with Tunable Color. *Journal of the American Ceramic Society* **2020**, *103* (11), 6280–6288. https://doi.org/10.1111/JACE.17339.

(24) Bondioli, F.; Bondioli, F.; Corradi, A. B.; Manfredini, T.; Leonelli, C. Nonconventional Synthesis of Praseodymium- Doped Ceria by Flux Method Nonconventional Synthesis of Praseodymium-Doped Ceria by Flux Method. **2015**, *33* (August), 324–330.

(25) Song, H. Z.; Wang, H. B.; Zha, S. W.; Peng, D. K.; Meng, G. Y. Aerosol-Assisted MOCVD Growth of Gd2O3-Doped CeO2 Thin SOFC Electrolyte Film on Anode Substrate. *Solid State Ion* **2003**, *156* (3–4), 249–254. https://doi.org/10.1016/S0167-2738(02)00688-4.

(26) Yulizar, Y.; Juliyanto, S.; Sudirman; Apriandanu, D. O. B.; Surya, R. M. Novel Sol-Gel Synthesis of CeO2 Nanoparticles Using Morinda Citrifolia L. Fruit Extracts: Structural and Optical Analysis. *J Mol Struct* **2021**, *1231*, 129904. https://doi.org/10.1016/J.MOLSTRUC.2021.129904.

(27) Maria Magdalane, C.; Kaviyarasu, K.; Siddhardha, B.; Ramalingam, G. Synthesis and Characterization of CeO2 Nanoparticles by Hydrothermal Method. *Mater Today Proc* **2021**, *36*, 130–132. https://doi.org/10.1016/J.MATPR.2020.02.283.

(28) Zhao, W.; Rong, J.; Luo, W.; Long, L.; Yao, X. Enhancing the K-Poisoning Resistance of CeO2-SnO2 Catalyst by Hydrothermal Method for NH3-SCR Reaction. *Appl Surf Sci* **2022**, *579*, 152176. https://doi.org/10.1016/J.APSUSC.2021.152176.

(29) Carregosa, J. D. C.; Grilo, J. P. F.; Godoi, G. S.; Macedo, D. A.; Nascimento, R. M.; Oliveira, R. M. P. B. Microwave-Assisted Hydrothermal Synthesis of Ceria (CeO2): Microstructure, Sinterability and Electrical Properties. *Ceram Int* **2020**, *46* (14), 23271–23275. https://doi.org/10.1016/J.CERAMINT.2020.06.021.

(30) Jin, W.; Liu, Y.; Yu, J.; Guo, X.; Mao, D. Effect of Copper Precursors on CO Oxidation Catalyzed by CuO-CeO2 Prepared by Solvothermal Method. *Journal of Rare Earths* **2022**. https://doi.org/10.1016/J.JRE.2022.10.005.

(31) Mishra, A. K.; Nayak, A. K.; Das, A. K.; Pradhan, D. Microwave-Assisted Solvothermal Synthesis of Cupric Oxide Nanostructures for High-Performance Supercapacitor. *Journal of Physical Chemistry C* **2018**, *122* (21), 11249–11261. https://doi.org/10.1021/acs.jpcc.8b02210.

(32) Mishra, S.; Soren, S.; Debnath, A. K.; Aswal, D. K.; Das, N.; Parhi, P. Rapid Microwave – Hydrothermal Synthesis of CeO2 Nanoparticles for Simultaneous Adsorption/Photodegradation of Organic Dyes under Visible Light. *Optik (Stuttg)* **2018**, *169*, 125–136. https://doi.org/10.1016/J.IJLEO.2018.05.045.

(33) Samiee, S.; Goharshadi, E. K. Effects of Different Precursors on Size and Optical Properties of Ceria Nanoparticles Prepared by Microwave-Assisted Method. *Mater Res Bull* **2012**, *47*, 1089–1095.

(34) Cavalcante, L. S.; Sczancoski, J. C.; Siu Li, M.; Longo, E.; Varela, J. A. β-ZnMoO4 Microcrystals Synthesized by the Surfactant-Assisted Hydrothermal Method: Growth Process and Photoluminescence Properties. *Colloids Surf A Physicochem Eng Asp* **2012**, *396*, 346–351. https://doi.org/10.1016/J.COLSURFA.2011.12.021.

(35) Komarneni, S.; Katsuki, H. Nanophase Materials by a Novel Microwave-Hydrothermal Process. *Pure and Applied Chemistry* **2002**, *74* (9), 1537–1543. https://doi.org/10.1351/PAC200274091537/MACHINEREADABLECITATION/RIS.

(36) Xie, S.; Wang, Z.; Cheng, F.; Zhang, P.; Mai, W.; Tong, Y. Ceria and Ceria-Based Nanostructured Materials for Photoenergy Applications. *Nano Energy* **2017**, *34*, 313–337. https://doi.org/10.1016/j.nanoen.2017.02.029.

(37) Kumar, A.; Kuang, Y.; Liang, Z.; Sun, X. Microwave Chemistry, Recent Advancements, and Eco-Friendly Microwave-Assisted Synthesis of Nanoarchitectures and Their Applications: A Review. *Mater Today Nano* **2020**, *11*, 100076. https://doi.org/10.1016/J.MTNANO.2020.100076.

(38) Schmink, J. R.; Leadbeater, N. E. *Microwave Heating as a Tool for Sustainable Chemistry - Google Books*; 2010.

(39) Deus, R. C.; Cilense, M.; Foschini, C. R.; Ramirez, M. A.; Longo, E.; Simões, A. Z. Influence of Mineralizer Agents on the Growth of Crystalline CeO2 Nanospheres by the Microwave-Hydrothermal Method. *J Alloys Compd* **2013**, *550*, 245–251. https://doi.org/10.1016/J.JALLCOM.2012.10.001.

(40) Amoresi, R. A. C.; Oliveira, R. C.; Marana, N. L.; de Almeida, P. B.; Prata, P. S.; Zaghete, M. A.; Longo, E.; Sambrano, J. R.; Simões, A. Z. CeO2 Nanoparticle Morphologies and Their Corresponding Crystalline Planes for the Photocatalytic Degradation of Organic Pollutants. *ACS Appl Nano Mater* **2019**, *2* (10), 6513–6526. https://doi.org/10.1021/ACSANM.9B01452/ASSET/IMAGES/LARGE/AN9B01452_0008.JPEG.

(41) de Oliveira, R. C.; Amoresi, R. A. C.; Marana, N. L.; Zaghete, M. A.; Ponce, M.; Chiquito, A. J.; Sambrano, J. R.; Longo, E.; Simões, A. Z. Influence of Synthesis Time on the Morphology and Properties of CeO2Nanoparticles: An Experimental-Theoretical Study. *Cryst Growth Des* **2020**, *20* (8), 5031–5042. https://doi.org/10.1021/acs.cgd.0c00165.

(42) Ortega, P. P.; Hangai, B.; Moreno, H.; Rocha, L. S. R.; Ramírez, M. A.; Ponce, M. A.; Longo, E.; Simões, A. Z. Tuning Structural, Optical, and Gas Sensing Properties of Ceria-Based Materials by Rare-Earth Doping. *J Alloys Compd* **2021**, *888*, 161517. https://doi.org/10.1016/J.JALLCOM.2021.161517.

(43) Oliveira, L. L.; Cortés, J. A.; Caldeira, B. S.; Strusch, T.; Wiedwald, U.; Simoes, A. Z. Structural, Electronic Paramagnetic Resonance and Magnetic Properties of Praseodymium-Doped Rare Earth CeO2 Semiconductors. *Ceram Int* **2021**, *47* (15), 20768–20780. https://doi.org/10.1016/J.CERAMINT.2021.04.133.

(44) Byzynski, G.; Melo, C.; Volanti, D. P.; Ferrer, M. M.; Gouveia, A. F.; Ribeiro, C.; Andrés, J.; Longo, E. The Interplay between Morphology and Photocatalytic Activity in ZnO and N-Doped ZnO Crystals. *Mater Des* **2017**, *120*, 363–375. https://doi.org/10.1016/J.MATDES.2017.02.020.

(45) Trench, A. B.; Machado, T. R.; Gouveia, A. F.; Assis, M.; da Trindade, L. G.; Santos, C.; Perrin, A.; Perrin, C.; Oliva, M.; Andrés, J.; Longo, E. Connecting Structural, Optical, and Electronic Properties and Photocatalytic Activity of Ag3PO4:Mo Complemented by DFT Calculations. *Appl Catal B* **2018**, *238*, 198–211. https://doi.org/10.1016/J.APCATB.2018.07.019.

(46) Roca, R. A.; Sczancoski, J. C.; Nogueira, I. C.; Fabbro, M. T.; Alves, H. C.; Gracia, L.; Santos, L. P. S.; de Sousa, C. P.; Andrés, J.; Luz, G. E.; Longo, E.; Cavalcante, L. S. Facet-Dependent Photocatalytic and Antibacterial Properties of α-Ag2WO4 Crystals: Combining Experimental Data and Theoretical Insights. *Catal Sci Technol* **2015**, *5* (8), 4091–4107. https://doi.org/10.1039/C5CY00331H.

(47) Macedo, N. G.; Gouveia, A. F.; Roca, R. A.; Assis, M.; Gracia, L.; Andrés, J.; Leite, E. R.; Longo, E. Surfactant-Mediated Morphology and Photocatalytic Activity of α-Ag2WO4 Material. *Journal of Physical Chemistry C* **2018**, *122* (15), 8667–8679. https://doi.org/10.1021/ACS.JPCC.8B01898/ASSET/IMAGES/MEDIUM/JP-2018-01898X_M005.GIF.

(48) Bomio, M. R. D.; Tranquilin, R. L.; Motta, F. v.; Paskocimas, C. A.; Nascimento, R. M.; Gracia, L.; Andres, J.; Longo, E. Toward Understanding the Photocatalytic Activity of PbMoO4 Powders with Predominant (111), (100), (011), and (110) Facets. A Combined Experimental and Theoretical Study. *Journal of Physical Chemistry C* **2013**, *117* (41), 21382–21395. https://doi.org/10.1021/JP407416H/SUPPL_FILE/JP407416H_SI_001.PDF.

(49) Pereira, P. F. S.; Gouveia, A. F.; Assis, M.; de Oliveira, R. C.; Pinatti, I. M.; Penha, M.; Gonçalves, R. F.; Gracia, L.; Andrés, J.; Longo, E. ZnWO4 Nanocrystals: Synthesis, Morphology, Photoluminescence and Photocatalytic Properties. *Physical Chemistry Chemical Physics* **2018**, *20* (3), 1923–1937. https://doi.org/10.1039/c7cp07354b.

(50) F Gouveia, A.; Assis, M.; S Cavalcante, L.; Longo, E.; Andrés, J. Reading at Exposed Surfaces: Theoretical Insights into Photocatalytic Activity of ZnWO4. *Frontier Research Today* **2018**, *1*, 1005. https://doi.org/10.31716/FRT.201801005.

(51) Bai, L.; Wu, Y.; Zhang, L. Influence of FeNb Codoping on the Dielectric and Electrical Properties of CaCu3Ti4O12ceramics. *J Alloys Compd* **2016**, *661*, 6–13. https://doi.org/10.1016/j.jallcom.2015.11.142.

(52) Huang, M. H. Facet-Dependent Optical Properties of Semiconductor Nanocrystals. *Small* **2019**, *15* (7), 1804726. https://doi.org/10.1002/SMLL.201804726.

(53) Rietveld, H. M. A Profile Refinement Method for Nuclear and Magnetic Structures. *J Appl Crystallogr* **1969**, *2* (2), 65–71. https://doi.org/10.1107/s0021889869006558.

(54) Coelho, A. A. TOPAS and TOPAS-Academic: An Optimization Program Integrating Computer Algebra and Crystallographic Objects Written in C++. *J Appl Crystallogr* **2018**, *51* (1), 210–218. https://doi.org/10.1107/S1600576718000183.

(55) Cavalcante, L. S.; Moraes, E.; Almeida, M. A. P.; Dalmaschio, C. J.; Batista, N. C.; Varela, J. A.; Longo, E.; Siu Li, M.; Andrés, J.; Beltrán, A. A Combined Theoretical and Experimental Study of Electronic Structure and Optical Properties of β-ZnMoO4 Microcrystals. *Polyhedron* **2013**, *54*, 13–25. https://doi.org/10.1016/J.POLY.2013.02.006.

(56) Dovesi, R.; Orlando, R.; Erba, A.; Zicovich-Wilson, C. M.; Civalleri, B.; Casassa, S.; Maschio, L.; Ferrabone, M.; de La Pierre, M.; D'Arco, P.; Noël, Y.; Causà, M.; Rérat, M.; Kirtman, B. CRYSTAL14: A Program for the Ab Initio Investigation of Crystalline Solids. *Int J Quantum Chem* **2014**, *114* (19), 1287–1317. https://doi.org/10.1002/QUA.24658.

(57) Adamo, C.; Barone, V. Toward Reliable Density Functional Methods without Adjustable Parameters: The PBE0 Model. *J Chem Phys* **1999**, *110* (13), 6158. https://doi.org/10.1063/1.478522.

(58) Barmparis, G. D.; Lodziana, Z.; Lopez, N.; Remediakis, I. N. Nanoparticle Shapes by Using Wulff Constructions and First-Principles Calculations. *Beilstein Journal of Nanotechnology* **2015**, *6* (1), 361–368. https://doi.org/10.3762/bjnano.6.35.

(59) Laier, L. O.; Assis, M.; Foggi, C. C.; Gouveia, A. F.; Vergani, C. E.; Santana, L. C. L.; Cavalcante, L. S.; Andrés, J.; Longo, E. Surface-Dependent Properties of α-Ag2WO4: A Joint Experimental and Theoretical Investigation. *Theor Chem Acc* **2020**, *139* (7). https://doi.org/10.1007/s00214-020-02613-z.

(60) de Foggi, C. C.; Oliveira, R. C.; Assis, M.; Fabbro, M. T.; Mastelaro, V. R.; Vergani, C. E.; Gracia, L.; Andrés, J.; Longo, E.; Machado, A. L. Unvealing the Role of B-Ag2MoO4 Microcrystals to the Improvement of Antibacterial Activity. *Materials Science & Engineering C* **2020**, *111*, 110765.

(61) Assis, M.; de Foggi, C. C.; Teodoro, V.; de Campos da Costa, J. P.; Silva, C. E.; Robeldo, T.; Caperucci, P. F.; Vergani, C. E.; Borra, R. C.; Sorribes, I.; Gouveia, A. F.; San-Miguel, M. A.; Andrés, J.; Longo, E. Surface-Dependent Photocatalytic and Biological Activities of Ag2CrO4: Integration of Experiment and Simulation. *Appl Surf Sci* **2021**, *545* (October 2020). https://doi.org/10.1016/j.apsusc.2021.148964.

(62) Assis, M.; Tello, A. C. M.; Abud, F. S. A.; Negre, P.; Ribeiro, L. K.; Ribeiro, R. A. P.; Masunaga, S. H.; Lima, A. E. B.; Luz Júnior, G. E.; Jardim, R. F.; da Silva, A. B. F.; Andrés, J.; Longo, E. Bridging Experiment and Theory: Morphology, Optical, Electronic, and Magnetic Properties of MnWO4. *Appl Surf Sci* **2022**, *600*, 154081.

(63) Monkhorst, H. J.; Pack, J. D. Special Points for Brillouin-Zone Integrations. *Phys Rev B* **1976**, *13* (12), 5188. https://doi.org/10.1103/PhysRevB.13.5188.

(64) Jaffe, J. E.; Hess, A. C. Hartree-Fock Study of Phase Changes in ZnO at High Pressure. *Phys Rev B* **1993**, *48* (11), 7903. https://doi.org/10.1103/PhysRevB.48.7903.

(65) Dhara, A.; Sain, S.; Sadhukhan, P.; Das, S.; Kumar, S. Effect of Lattice Distortion in Optical Properties of CeO 2 Nanocrystals on Mn Substitution by Mechanical Alloying. *J Alloys Compd* **2019**, *786*, 215–224. https://doi.org/10.1016/j.jallcom.2019.01.350.

(66) Shannon, R. D. Revised Effective Ionic Radii and Systematic Studies of Interatomic Distances in Halides and Chalcogenides. *Acta Crystallogr* **1976**, *A32*, 751–767.

(67) Khan, M. A. M.; Khan, W.; Ahamed, M.; Alhazaa, A. N. Microstructural Properties and Enhanced Photocatalytic Performance of Zn Doped CeO2 Nanocrystals. *Scientific Reports 2017 7:1* **2017**, *7* (1), 1–11. https://doi.org/10.1038/s41598-017-11074-7.

(68) Zhang, Y. W.; Si, R.; Liao, C. S.; Yan, C. H.; Xiao, C. X.; Kou, Y. Facile Alcohothermal Synthesis, Size-Dependent Ultraviolet Absorption, and Enhanced CO Conversion Activity of Ceria Nanocrystals. *Journal of Physical Chemistry B* **2003**, *107* (37), 10159–10167. https://doi.org/10.1021/jp034981o.

(69) Kanakaraju, S.; Mohan, S.; Sood, A. K. Optical and Structural Properties of Reactive Ion Beam Sputter Deposited CeO2 Films. *Thin Solid* **1997**, *305*, 191–195.

(70) Nurhasanah, I.; Abdullah, M.; Khairurrijal. Structure and Morphology of Neodymium-doped Cerium Oxide Solid Solution Prepared by a Combined Simple Polymer Heating and

D.C.-Magnetron Sputtering Method. *AIP Conf Proc* **2008**, *989* (1), 147. https://doi.org/10.1063/1.2906051.

(71) Deus, R. C.; Amoresi, R. A. C.; Desimone, P. M.; Schipani, F.; Rocha, L. S. R.; Ponce, M. A.; Simoes, A. Z.; Longo, E. Electrical Behavior of Cerium Dioxide Films Exposed to Different Gases Atmospheres. *Ceram Int* **2016**, *42* (13), 15023–15029. https://doi.org/10.1016/J.CERAMINT.2016.06.151.

(72) Wu, L.; Wiesmann, H. J.; Moodenbaugh, A. R.; Klie, R. F.; Zhu, Y.; Welch, D. O.; Suenaga, M. Oxidation State and Lattice Expansion of CeO2-x Nanoparticles as a Function of Particle Size. *Phys Rev B Condens Matter Mater Phys* **2004**, *69* (12), 1–9. https://doi.org/10.1103/PhysRevB.69.125415.

(73) Moreno, O. P.; Pérez, R. G.; Merino, R. P.; Portillo, M. C.; Tellez, G. H.; Rosas, E. R.; Tototzintle, M. Z. CeO2 Nanoparticles Growth by Chemical Bath and Its Thermal Annealing Treatment in Air Atmosphere. *Optik (Stuttg)* **2017**, *148*, 142–150.

(74) Chen, H.-I.; Chang, H.-Y. Synthesis and Characterization of Nanocrystalline Cerium Oxide Powders by Two-Stage Non-Isothermal Precipitation. *Solid State Commun* **2005**, *133*, 593–598.

(75) Golubović, A.; Šćepanović, M.; Kremenović, A.; Aškrabić, S.; Berec, V.; Dohčević-Mitrović, Z.; Popović, Z. v. Raman Study of the Variation in Anatase Structure of TiO2 Nanopowders Due to the Changes of Sol-Gel Synthesis Conditions. *J Solgel Sci Technol* **2009**, *49* (3), 311–319. https://doi.org/10.1007/S10971-008-1872-3/FIGURES/9.

(76) Campbell, I. H.; Fauchet, P. M. The Effects of Microcrystal Size and Shape on the One Phonon Raman Spectra of Crystalline Semiconductors. *Solid State Commun* **1986**, *58* (10), 739–741. https://doi.org/10.1016/0038-1098(86)90513-2.

(77) Torrente-Murciano, L.; Gilbank, A.; Puertolas, B.; Garcia, T.; Solsona, B.; Chadwick, D. Shape-Dependency Activity of Nanostructured CeO2 in the Total Oxidation of Polycyclic Aromatic Hydrocarbons. *Appl Catal B* **2013**, *132–133*, 116–122. https://doi.org/10.1016/j.apcatb.2012.10.030.

(78) Tao, Y.; Wang, H.; Xia, Y.; Zhang, G.; Wu, H.; Tao, G. Preparation of Shape-Controlled CeO2 Nanocrystals via Microwave-Assisted Method. *Mater Chem Phys* **2010**, *124* (1), 541–546. https://doi.org/10.1016/j.matchemphys.2010.07.007.

(79) Zawadzki, M. Preparation and Characterization of Ceria Nanoparticles by Microwave-Assisted Solvothermal Process. *J Alloys Compd* **2008**, *454* (1–2), 347–351. https://doi.org/10.1016/j.jallcom.2006.12.078.

(80) Banoth, P.; Sohan, A.; Kandula, C.; Kanaka, R. K.; Kollu, P. Microwave-Assisted Solvothermal Route for One-Step Synthesis of Pure Phase Bismuth Ferrite Microflowers with Improved Magnetic and Dielectric Properties. *ACS Omega* **2022**, *7* (15), 12910–12921. https://doi.org/10.1021/acsomega.2c00219.

(81) Xu, L.; Hu, Y. L.; Pelligra, C.; Chen, C. H.; Jin, L.; Huang, H.; Sithambaram, S.; Aindow, M.; Joesten, R.; Suib, S. L. ZnO with Different Morphologies Synthesized by Solvothermal Methods for Enhanced Photocatalytic Activity. *Chemistry of Materials* **2009**, *21* (13), 2875–2885. https://doi.org/10.1021/cm900608d.

(82) Wolf, M. J.; Kullgren, J.; Broqvist, P.; Hermansson, K. Fluorine Impurities at CeO2(111): Effects on Oxygen Vacancy Formation, Molecular Adsorption, and Surface Re-Oxidation. *Journal of Chemical Physics* **2017**, *146* (4). https://doi.org/10.1063/1.4973239.

(83) Ananchuensook, A.; Wongchoosuk, C.; T-Thienprasert, J.; Boonchun, A.; Jungthawan, S.; Reunchan, P. Effects of Oxygen Pressure on the Morphology and Surface Energetics of β-PbO2: Insight from DFT Calculations. *Physical Chemistry Chemical Physics* **2022**. https://doi.org/10.1039/d2cp04632f.

(84) Mochizuki, S.; Fujishiro, F. The Photoluminescence Properties and Reversible Photoinduced Spectral Change of CeO2 Bulk, Film and Nanocrystals. *physica status solidi (b)* **2009**, *246* (10), 2320–2328. https://doi.org/10.1002/PSSB.200844419.

(85) Yu, S. H.; Cölfen, H.; Fischer, A. High Quality CeO2 Nanocrystals Stabilized by a Double Hydrophilic Block Copolymer. *Colloids Surf A Physicochem Eng Asp* **2004**, *243* (1–3), 49–52. https://doi.org/10.1016/J.COLSURFA.2004.05.006.

(86) Dorenbos, P. A Review on How Lanthanide Impurity Levels Change with Chemistry and Structure of Inorganic Compounds. *ECS Journal of Solid State Science and Technology* **2013**, *2* (2), R3001–R3011. https://doi.org/10.1149/2.001302jss.

(87) Asami, K.; Ueda, J.; Shiraiwa, M.; Fujii, K.; Yashima, M.; Tanabe, S. Redshift and Thermal Quenching of Ce3+ Emission in (Gd, Y)3(Al, Si)5(O, N)12 Oxynitride Garnet Phosphors. *Opt Mater (Amst)* **2019**, *87*, 117–121. https://doi.org/10.1016/J.OPTMAT.2018.04.049.

(88) Das, D.; Gupta, S. K.; Sudarshan, K. Europium Luminescence as a Structural Probe to Understand Defect Evolution in CeO2/Eu3+, M3+ (M = Y and La): Contrasting Role of Codopant Ionic Size. *J Mater Sci* **2021**, *56* (30), 17205–17220. https://doi.org/10.1007/S10853-021-06366-3/TABLES/4.

(89) Dong, L.; Zhao, E.; Chen, Y.; Qin, G.; Xu, W. Impact of LED Color Temperatures on Perception Luminance in the Interior Zone of a Tunnel Considering Fog Transmittance. *Advances in Civil Engineering* **2020**, *2020*. https://doi.org/10.1155/2020/3971256.

(90) Lima, A. E. B.; Reis, R. Y. N.; Ribeiro, L. S.; Ribeiro, L. K.; Assis, M.; Santos, R. S.; Fernandes, C. H. M.; Cavalcante, L. S.; Longo, E.; Osajima, J. A. O.; Luz, G. E. Microwave-Assisted Hydrothermal Synthesis of CuWO4-Palygorskite Nanocomposite for Enhanced Visible Photocatalytic Response. *J Alloys Compd* **2021**, *863*, 158731. https://doi.org/10.1016/j.jallcom.2021.158731.

(91) Lemos, S. C. S.; Al., E. Efficient Ni and Fe Doping Process in ZnO with Enhanced Photocatalytic Activity: A Theoretical and Experimental Investigation. *Mater Res Bull* **2022**, *152*, 111849.

(92) Gao, W.; Ran, C.; Wang, M.; Li, L.; Sun, Z.; Yao, X. The Role of Reduction Extent of Graphene Oxide in the Photocatalytic Performance of Ag/AgX (X = Cl, Br)/RGO Composites and the Pseudo-Second-Order Kinetics Reaction Nature of the Ag/AgBr System. *Physical Chemistry Chemical Physics* **2016**, *18* (27), 18219–18226. https://doi.org/10.1039/c6cp03110b.

(93) Su, F.; Li, P.; Huang, J.; Gu, M.; Liu, Z.; Xu, Y. Photocatalytic Degradation of Organic Dye and Tetracycline by Ternary Ag2O/AgBr–CeO2 Photocatalyst under Visible-Light Irradiation. *Sci Rep* **2021**, *11* (1), 1–13. https://doi.org/10.1038/s41598-020-76997-0.

(94) Tuyen, L. T. T.; Quang, D. A.; Toan, T. T. T.; Tung, T. Q.; Hoa, T. T.; Mau, T. X.; Khieu, D. Q. Synthesis of CeO2/TiO2 Nanotubes and Heterogeneous Photocatalytics Degradation of Methylene Blue. *J Environ Chem Eng* **2018**, *6*, 5999–6011.

(95) Yu, B.; Meng, F.; Zhou, T.; Fan, A.; Zhao, Z.; Wasim Khan, M. Construction of CoS/CeO2 Heterostructure Nanocages with Enhanced Photocatalytic Performance under Visible Light. *Journal of the American Ceramic Society* **2020**, *103* (11), 6136–6148. https://doi.org/10.1111/jace.17340.

(96) Mandal, R. K.; Pradhan, S. K. Enhanced Photocatalytic Performance of Cauliflower-like CeO2-TiO2 Nancomposite for the RhB Dye Degradation under Visible Light. *Mater Today Proc* **2022**, *66*, 3307–3314.

(97) Wangkawong, K.; Phanichphant, S.; Tantraviwat, D.; Inceesungvorn, B. Photocatalytic Efficiency Improvement of Z-Scheme CeO2/BoOI Heterostructure for RHB Degradation and Benzylamine Oxidation under Visible Light Irradiation. *J Taiwan Inst Chem Eng* **2020**, *108*, 55–63.

(98) Assis, M.; Robeldo, T.; Foggi, C. C.; Kubo, A. M.; Mínguez-Vega, G.; Condoncillo, E.; Beltran-Mir, H.; Torres-Mendieta, R.; Andrés, J.; Oliva, M.; Vergani, C. E.; Barbugli, P. A.; Camargo, E. R.; Borra, R. C.; Longo, E. Ag Nanoparticles/α-Ag2WO4 Composite Formed by Electron Beam and Femtosecond Irradiation as Potent Antifungal and Antitumor Agents. *Sci Rep* **2019**, *9* (1), 1–15. https://doi.org/10.1038/s41598-019-46159-y.

(99) de Jesus Silva Chaves, M.; de Oliveira Lima, G.; de Assis, M.; de Jesus Silva Mendonça, C.; Pinatti, I. M.; Gouveia, A. F.; Viana Rosa, I. L.; Longo, E.; Almeida, M. A. P.; Rodrigues dos Santos Franco, T. C. Environmental Remediation Properties of Bi 2 WO 6 Hierarchical Nanostructure: A Joint Experimental and Theoretical Investigation. *J Solid State Chem* **2019**, *274* (August 2018), 270–279. https://doi.org/10.1016/j.jssc.2019.03.031.

(100) Assis, M.; de Foggi, C. C.; Teodoro, V.; da Costa, J. P. C.; Silva, C. E.; Robeldo, T.; Caperucci, P. F.; Vergani, C. E.; Borra, R. C.; Sorribes, I.; Gouveia, A. F.; San-Miguel, M. A.; Andrés, J.; Longo, E. Surface-Dependent Photocatalytic and Biological Activities of Ag2CrO4: Integration of Experiment and Simulation. *Appl Surf Sci* **2021**, *545*, 148964.

(101) Ribeiro, L. K.; Gouveia, A. F.; Silva, F. das C. M.; Noleto, L. F. G.; Assis, M.; Batista, A. M.; Cavalcante, L. S.; Guillamón, E.; Rosa, I. L. V.; Longo, E.; Andrés, J.; Luz Júnior, G. E. Tug-of-War Driven by the Structure of Carboxylic Acids: Tuning the Size, Morphology,

and Photocatalytic Activity of α-Ag2WO4. *Nanomaterials* **2022**, *12* (19), 1–12. https://doi.org/10.3390/nano12193316.

(102) Tello, A. C. M.; Assis, M.; Menasce, R.; Gouveia, A. F.; Teodoro, V.; Jacomaci, N.; Zaghete, M. A.; Andrés, J.; Marques, G. E.; Teodoro, M. D.; da Silva, A. B. F.; Longo, E. Microwave-Driven Hexagonal-to-Monoclinic Transition in BiPO4: An In-Depth Experimental Investigation and First-Principles Study. *Inorg Chem* **2020**, *59* (11), 7453–7468. https://doi.org/10.1021/acs.inorgchem.0c00181.

(103) Assis, M.; Groppo Filho, F. C.; Pimentel, D. S.; Robeldo, T.; Gouveia, A. F.; Castro, T. F. D.; Fukushima, H. C. S.; de Foggi, C. C.; da Costa, J. P. C.; Borra, R. C.; Andrés, J.; Longo, E. Ag Nanoparticles/AgX (X=Cl, Br and I) Composites with Enhanced Photocatalytic Activity and Low Toxicological Effects. *ChemistrySelect* **2020**, *5* (15), 4655–4673. https://doi.org/10.1002/slct.202000502.

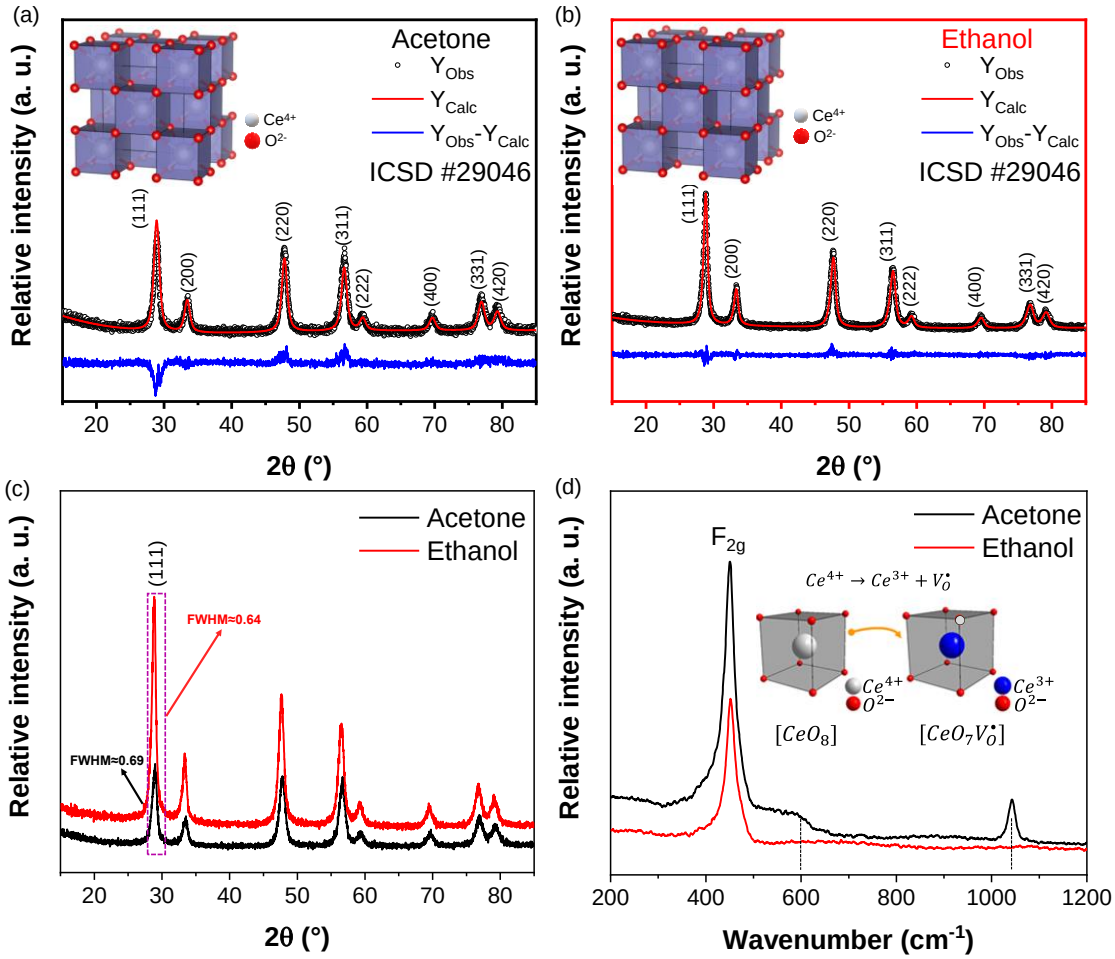

Figure 1 - *Rietveld* analysis for the CeO_2 samples synthesized by MAS using (a) acetone and (b) ethanol. (*c*) Raman spectra for the CeO_2 samples synthesized via MAS using acetone and ethanol.

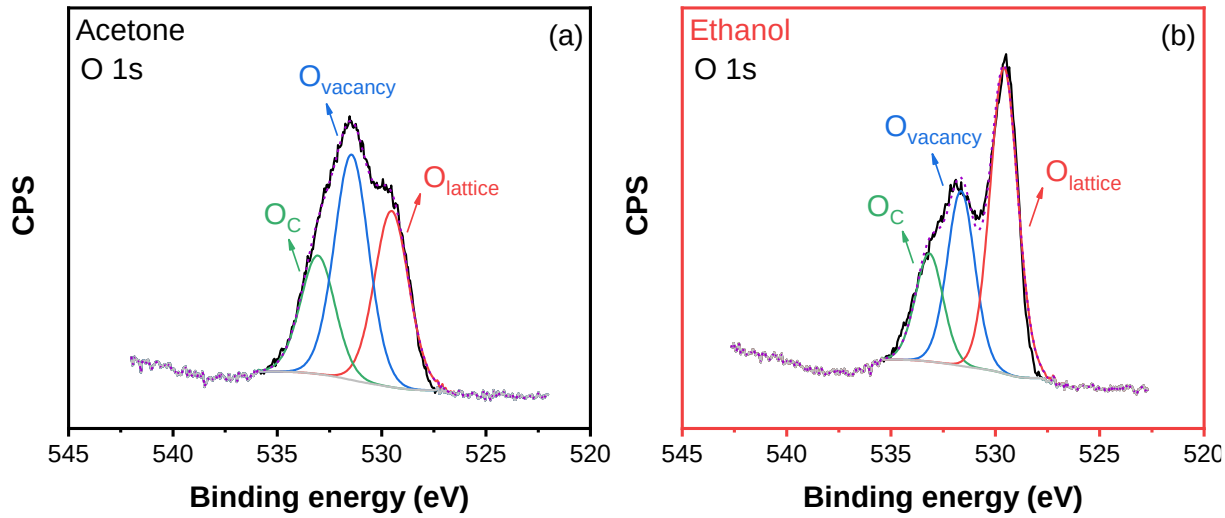

Figure 2 – O 2p XPS peak fitting for the samples synthesized in acetone and ethanol.

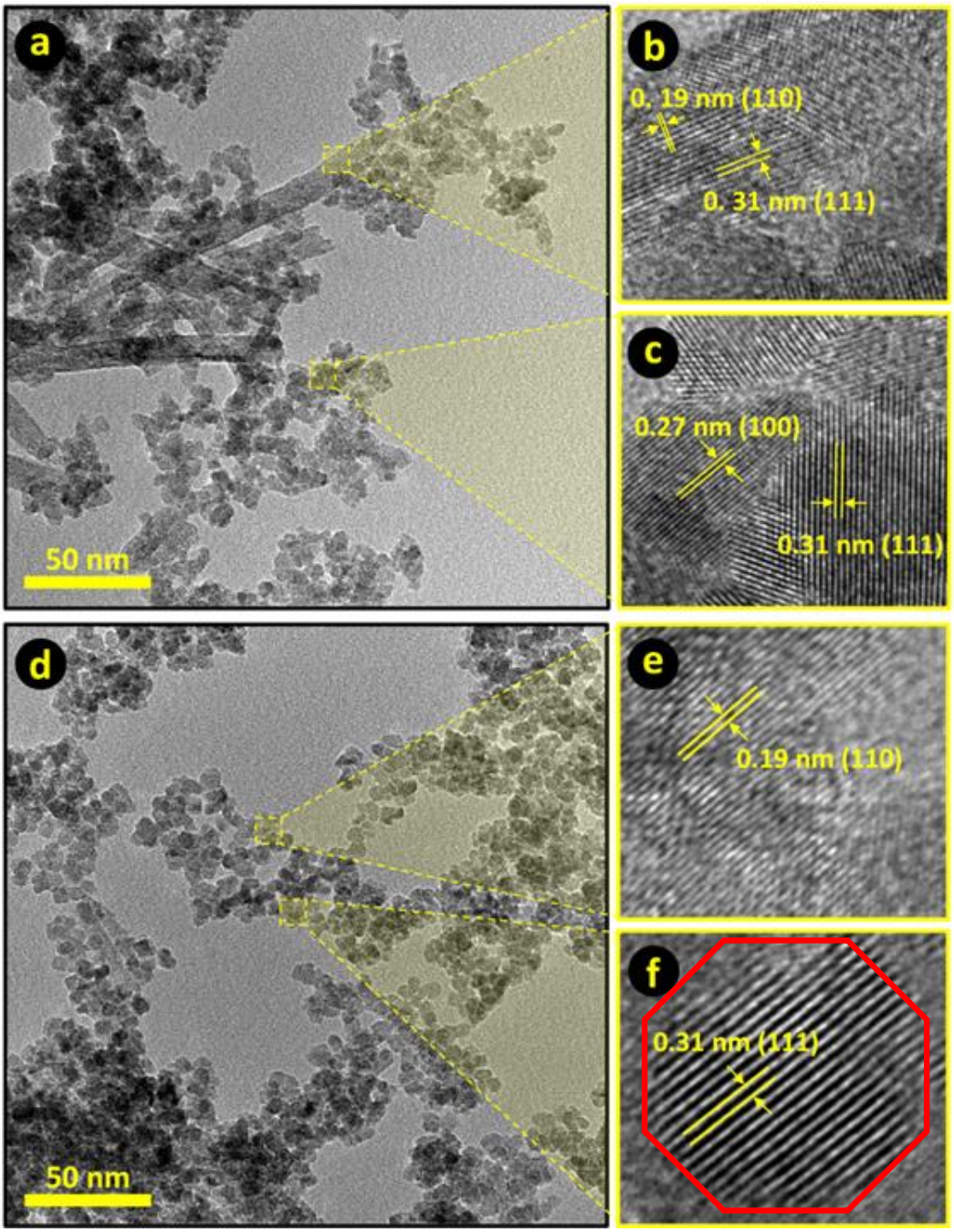

Figure 3 – TEM and HRTEM micrograph images for the CeO_2 samples synthesized via MAS in (a-c) acetone and (d-f) ethanol.

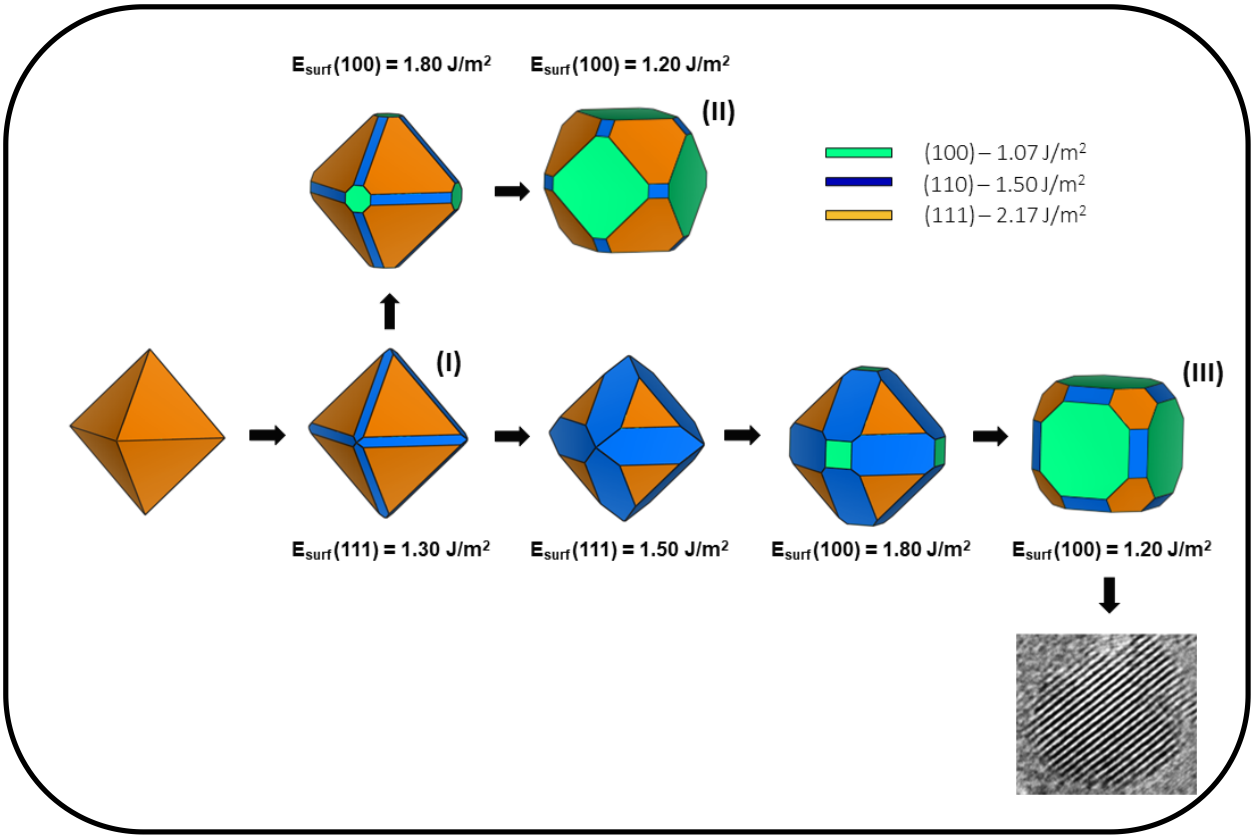

Figure 4 - Crystallographic structure based on Wulff constructions for CeO_2 with crystal planes (111), (110) and (100).

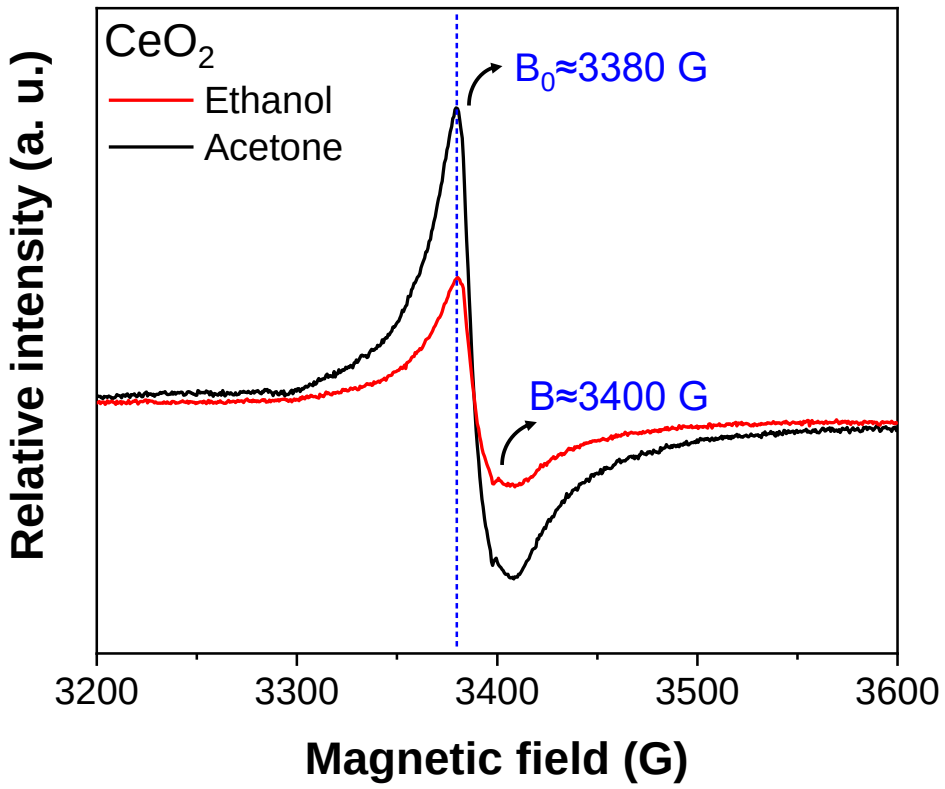

Figure 5 - EPR spectra for CeO_2 samples synthesized via MAS in ethanol and acetone.

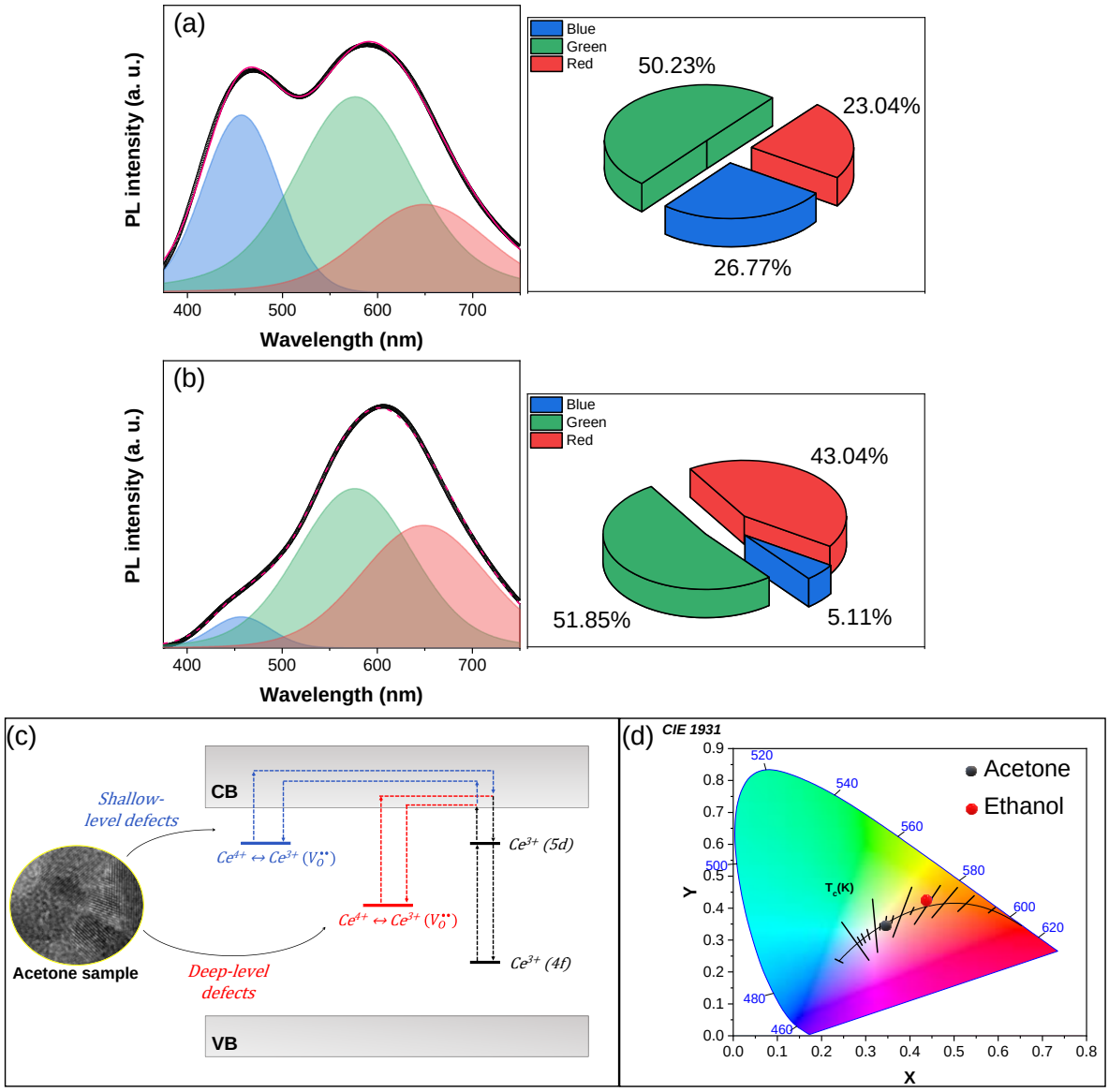

Figure 6 – PL spectrum deconvolution for the CeO_2 samples synthesized via MAS in (a) acetone and (b) ethanol. The (c) proposed electronic structure model/emission mechanism, and (d) chromaticity diagram (CIE 1931) for the CeO_2 samples synthesized via MAS in (a) acetone and (b) ethanol.

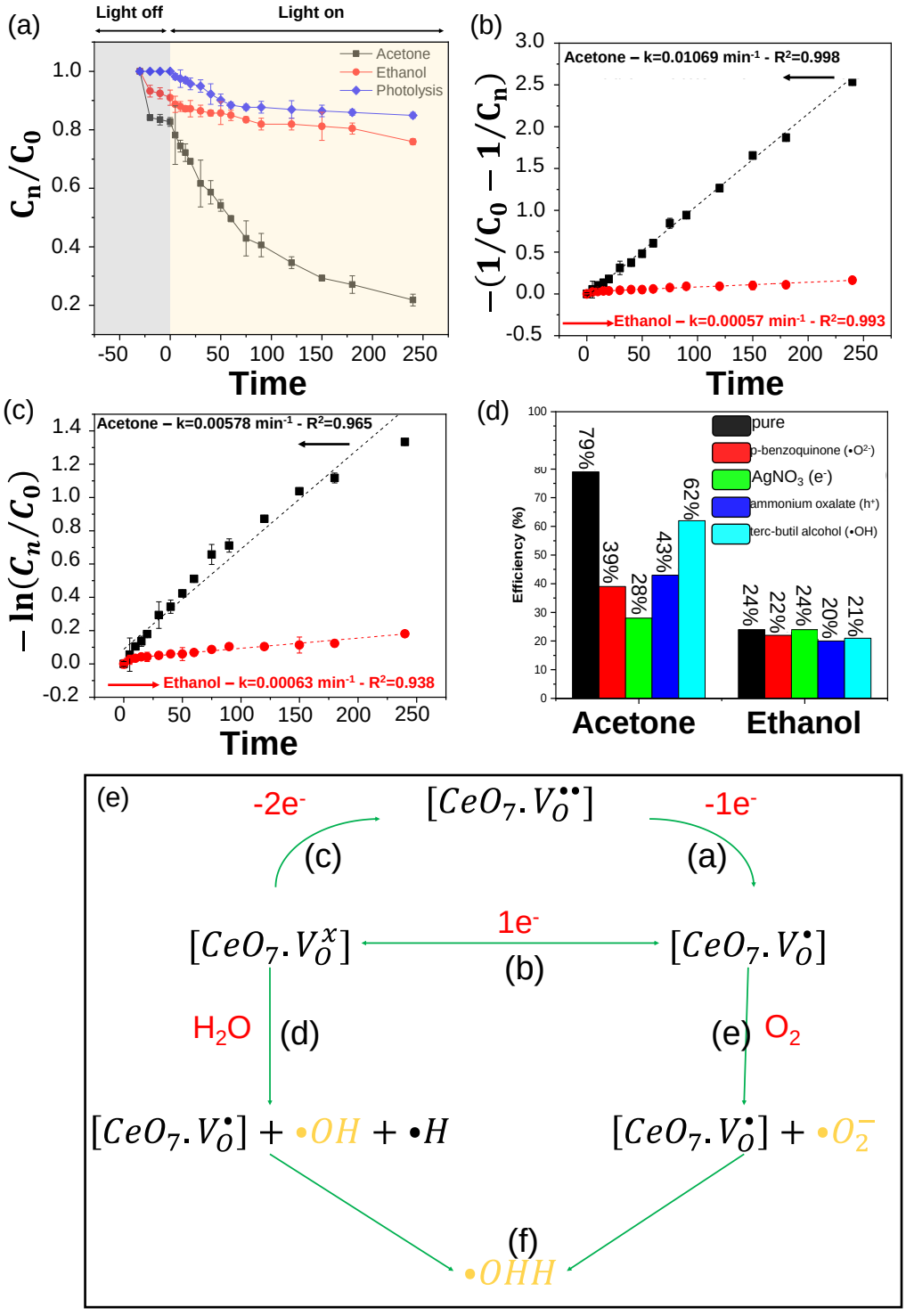

Figure 7 – (a) CeO_2 samples photocatalytic behavior; Photocatalysis results with kinetics adjustments using the (b) pseudo-second order model, and (c) pseudo-first order model, respectively. (d) Scavengers test for the CeO_2 samples, and (e) possible ROS generation mechanism.

Table 1 - Structural and Rietveld parameters, specific surface area Brunauer–Emmett–Teller (BET) and adsorption pore diameter values, and gas sensing response and recovery time for the CeO_2 samples synthesized by MAS using acetone and ethanol.

Sample	CeO_2			Rietveld parameters					S_{BET} (m^2/g)
	V ($Å^3$)	C. size(nm)	phase (%)	R_{bragg}	R_{exp}	R_{wp}	R_p	χ^2	
Acetone	160.1 ± 0.8	14.2 ± 1.1	100.0	9.70	9.27	13.00	10.39	1.40	130.98
Ethanol	159.8 ± 0.8	20.7 ± 0.8	100.0	2.10	6.09	5.23	4.10	0.86	121.29

Table 2 - Comparison of degradation efficiencies.

Photocatalyst	Method	Source/power (W)	Degradant	$[C]_{org}$ (mg L^{-1})	$[C]_{cat}$ (mg mL^{-1})	Time (min)	k (min^{-1})	η (%)	Ref.
$Ag_2O/AgBr–CeO_2$	CP/SC	Visible/500	RhB/TC	10/10	0.5	60	0.00182	95.6/93.23	Su, 2021
CeO_2-MOFs	(PA-DBD)	UV/500	MO	50	0.8	36	0.16021	98.0	Tao, 2019
CeO_2/TiO_2	HM	Visible/250	MB	15	1	120	0.032	100.0	Tuyen, 2018
CoS/CeO_2	Growing in-situ	Visible/300	TC/Phenol	25	40	60	0.06/0.037	96.5/90.5	Yu, 2020
CeO_2/CN	HM	Visible/500	SFX	0.5	0.1	60	0.072	99.2	Liu, 2020
CeO_2-TiO_2	MA	Visible/200	RhB	4	0.02	240	0.0008924	63.0	Mandal, 2022
CeO_2/BiOI	CP	Visible/50	RhB	4.8	50	180	0.0138	95.4	Wangkawong, 2020
CeO_2/CdS	CP	Visible/350	RhB	10	1	180	0.036	96.16	Pei, 2022
Bi_2MoO_6/CeO_2	SM	Visible/300	RhB/TC	10	0.4	90	0.0352	73.8/94.1	Gao, 2022
Ag/CeO_2/graphene	SG/HM	Sono photocatalytic irradiation	MB	20	0.005	120		100.0	Mardani, 2020
CeO_2	MH	UV/15	RhB	4.8	0.3	240	0.00578	80	This work

Table of Contents Entry.

This study shows how the sythesis environment can affect long-/short-range disorder. Superior photocatalytic response was achieved on CeO_2 synthesized in acetone. A blue-shift in photoluminescent emissions reinforces the formation of shallow-level defects within the crystal lattice.